Available online at www.sciencedirect.com

ScienceDirect

Comput. Methods Appl. Mech. Engrg. 382 (2021) 113848

Computer methods in applied mechanics and engineering

www.elsevier.com/locate/cma

Fully decoupling geometry from discretization in the Bloch–Floquet finite element analysis of phononic crystals

S.J. van den Boom[1], F. van Keulen[2], A.M. Aragón*[,3]

Faculty of Mechanical, Maritime and Materials Engineering, Delft University of Technology, Mekelweg 2, 2628 CD, Delft, The Netherlands

Received 9 November 2020; received in revised form 30 March 2021; accepted 1 April 2021
Available online 3 May 2021

Abstract

An immersed enriched finite element method is proposed for the analysis of phononic crystals (PnCs) with finite element (FE) meshes that are completely decoupled from geometry. Particularly, a technique is proposed to prescribe Bloch–Floquet periodic boundary conditions *strongly* on non-matching edges of the periodic unit cell (PUC). The enriched finite element formulation effectively transforms a periodic non-confirming discretization into an enriched node-to-node periodic discretizations where periodicity is enforced by any standard procedure. The enriched formulation is also used to describe the interior material interface. This completely eliminates the tedious process of generating matching or fitted meshes during the design process, as it allows changing the inclusion's geometry as well as the PnC's lattice type without changing the FE mesh. The proposed approach, which is used to analyze phononic crystals in 1-D, 2-D, and 3-D using structured meshes, exhibits the same performance as the standard finite element analysis on fitted meshes.

Keywords: Phononic crystals; Bloch–Floquet periodic boundary conditions; Unfitted/non-matching meshes; Enriched FEM; IGFEM/HIFEM; XFEM/GFEM

1. Introduction

Efficient analysis of phononic crystals (PnCs) is essential to their design for engineering applications. Specifically, computational design and optimization require the analysis of many variations of a design. In such cases, the fully immersed analysis of PnCs proposed in this work prevents the cumbersome procedure of generating matching meshes. As in the proposed method Bloch–Floquet boundary conditions are applied to non-matching edges in a *strong* manner, the lattice type as well as the inclusion can be altered without remeshing. Therefore, the computational design of PnCs is greatly simplified.

Phononic crystals have distinctive effects on waves traveling through them, and their design and optimization has therefore seen a recent increase in interest [1,2]. They exhibit bandgaps, *i.e.*, ranges of frequencies for which

---

* Corresponding author.
E-mail address: a.m.aragon@TUDelft.nl (A.M. Aragón).

[1] ORCID: 0000-0002-5547-2596

[2] ORCID: 0000-0003-2634-0110

[3] ORCID: 0000-0003-2275-6207

https://doi.org/10.1016/j.cma.2021.113848

no waves can propagate through the material due to Bragg scattering. A negative effective density and modulus can also be attained [3]. PnCs can be applied in many fields of engineering and across many length scales. For example, they can be used for thermal control [4] at one end of the frequency spectrum, and for seismic engineering at the other end [5]. New sensing schemes for liquids based on PnCs have also been introduced for biological samples and for hazardous chemicals such as gasoline [6,7]. Additional applications can be found in vibrationless environments for high-precision systems, sound protection devices, and acoustic waveguides and lenses [8]. Tuneable behavior may also be achieved: *in situ* changing of the impulse transmission can be achieved [9], and amplitude-tunable PnCs are optimized in [10]. Using a wave-like modulation of the constitutive parameters, symmetry and reciprocity of the wave propagation may even be broken [11].

In order to optimally utilize the full potential of PnCs, efficient and accurate models that capture the wave propagation properties are invaluable. Furthermore, methods for the systematic design of such crystals are required. For the analysis of PnCs, a large variety of modeling techniques is available. Examples are the Finite Element Method (FEM) [12], the Boundary Element Method (BEM) [13–15], Finite Differences - Time Domain (FDTD) [16,17], Plane Wave Expansion (PWE) technique [18,19], the monodromy matrix method [20,21], the Spectral Element Method (SEM) [22], IGA [23], and meshfree methods [24]. Homogenization approaches for the effective dynamic properties of PnCs are also being developed [25–27]. While all of these methods have advantages and disadvantages, FEM is widely used for complex geometries, as it extends effortlessly to inclusions of any shape. With FEM, periodic structures are generally studied by analyzing a PUC, whereby requiring the displacements at opposite sides of the PUC to be equal, periodicity is enforced. In the case of wave propagation problems, Bloch–Floquet periodic BCs are used instead; these impose a phase difference between both edges of the unit cell, and as a result they can describe traveling waves.

Despite the ease of implementation of standard FEM, it has a big disadvantage: the procedure calls for a *matching* (or *fitted* or *geometry-conforming*) mesh, *i.e.*, the edges of finite elements *must* align to material interfaces and PUC's sides. Creating such a mesh is undesirable in many situations, for instance during an iterative design process, where the unit cell geometry is not known *a priori*. Moreover, even when the geometry is known, the process of generating matching meshes is computationally expensive and prone to errors when complex geometries are involved. The issue of remeshing can be avoided completely by non-fitted or enriched finite element approaches. Wang et al. [28] have shown the use of a non-fitted Petrov–Galerkin interface approach for the analysis of PnCs. Similarly, the eXtended/Generalized Finite Element Method (X/GFEM) [29,30] provides a means to decouple material discontinuities from the FE discretization, by enriching the finite element formulation with discontinuous functions that are associated to nodes of intersected elements. For PnCs, this was demonstrated by Zhao et al. [31]. However, X/GFEM has many disadvantages: as enrichment functions do not vanish at original mesh nodes, their degrees of freedom (DOFs) do not retain their physical meaning. Therefore, essential (Dirichlet) boundary conditions generally need to be imposed *weakly*, *e.g.*, by means of Lagrange multipliers or the penalty method [32]. In the former case, positive definiteness of the system matrices is lost. Sanders et al. [33] discuss various methods for applying and stabilizing interface constraints. For the Bloch–Floquet periodic analysis of quantum-mechanical problems, Sukumar and Pask [34] proposed a formulation for classical and enriched finite element methods by constructing Bloch–Floquet periodic trial and test spaces. Additionally, X/GFEM can lead to ill-conditioned system matrices, which may be remedied by the use of Stable Generalized FEM (SGFEM) [35–37]. Lastly, the accuracy of the approximation in blending elements—elements for which not all nodes are enriched—may deteriorate [38].

There is another family of enriched finite element methods that can fully decouple the discretization from the problem's geometric features [39–43]; contrary to what is done in X/GFEM, enriched DOFs are collocated along discontinuities, eliminating many of the aforementioned issues. The Interface Enriched Generalized Finite Element Method (IGFEM) [39] was first proposed to solve problems with weak discontinuities, *i.e.*, where the gradient of the primal field is discontinuous as in problems containing perfectly bonded material interfaces. Enrichment functions in IGFEM are local to intersected elements by construction and they vanish at the original mesh nodes and at edges which are not crossed by material interfaces. As a result, Dirichlet boundary conditions are as straightforward to prescribe as in standard FEM. Dirichlet boundary conditions were prescribed weakly on enriched edges by Cuba-Ramos et al. [32], who first proposed IGFEM as an immersed (fictitious domain) method. In the context of computational design, the use of IGFEM for shape optimization has been shown for a range of engineering applications [44–47], and has been demonstrated for NURBS-based geometries as well [48]. Recently, IGFEM was also proposed for level-set based topology optimization [49]. The benefits of assigning enrichments to enriched

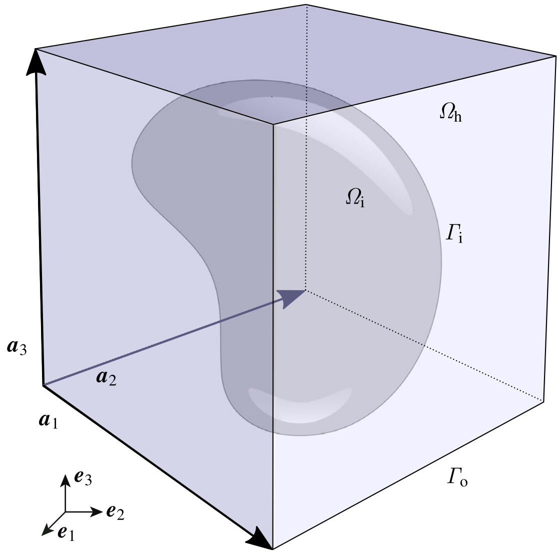

Fig. 1. Schematic representation of a PUC: a 3-D cube with lattice vectors $\boldsymbol{a}_1$, $\boldsymbol{a}_2$ and $\boldsymbol{a}_3$. The domain Ω consists of a host phase Ω_h and an inclusion Ω_i. The boundary between the two is denoted Γ_i, and Γ_o is the boundary of the PUC.

nodes along the discontinuities have inspired two important extensions to the method: the Hierarchical Interfaced-enriched Finite Element Method (HIFEM) [40], that can resolve multiple interfaces interacting within a single finite element, and the Discontinuity-Enriched Finite Element Method (DE-FEM) [41,42]. The latter is able to handle not only weak but also strong discontinuities—those where the field itself is discontinuous as in fracture problems—with a single unified formulation. DE-FEM inherits all assets of IGFEM and HIFEM, and in the absence of strong discontinuities (*e.g.*, cracks), it simplifies to these methods. Curved cracks and interfaces may also be analyzed using DE-FEM with NURBS-based discontinuities [50].

In this paper, which builds on the recently proposed immersed DE-FEM with strong enforcement of Dirichlet boundary conditions [43], we introduce the Interface-enriched Generalized Finite Element Method for the fully immersed analysis of PnCs, for which we derive a method for applying Bloch–Floquet BCs along non-matching PUC edges, similar to the strong enforcement of Dirichlet BCs introduced in [43]. We first verify the procedure by comparing the analytical and computed shear and pressure wave velocities obtained by means of an enriched immersed analysis of a homogeneous material. We then compare the convergence rates of IGFEM to those of standard FEM for a 1-D PnC and for the 2-D homogeneous PUCs, and demonstrate that the same rates of convergence are achieved for 2-D PnCs. Furthermore, we analyze a range of immersed 2-D phononic crystals with different lattice vectors, using the same background mesh, to demonstrate that full decoupling of mesh and PUC geometry is achieved. Finally, it is demonstrated that the formulation extends to complex 3-D phononic crystals, by means of an immersed cubic PUC with a "popcorn" shaped inclusion.

2. Problem formulation

In this work, we analyze PnCs by means of their periodic unit cell, represented by a d-dimensional parallelotope (line segment in 1-D, parallelogram in 2-D, or parallelepiped in 3-D). The PUC is replicated in d-dimensional space along the directions defined by lattice vectors $\boldsymbol{a}_i$, $i = \{1, \ldots, d\}$. The PUC, illustrated in Fig. 1, will be denoted by an open domain $\Omega \subset \mathbb{R}^d$. It is composed by a host phase Ω_h and an inclusion phase Ω_i, such that $\Omega_\mathrm{h} \cap \Omega_\mathrm{i} = \emptyset$; the closure of the domain is denoted $\overline{\Omega} = \overline{\Omega}_\mathrm{h} \cup \overline{\Omega}_\mathrm{i}$. The boundary of the domain Ω is given by $\partial\Omega \equiv \Gamma_\mathrm{o} = \overline{\Omega} \setminus \Omega$. We denote by Γ_i the interface separating the two material phases that is responsible for the weak discontinuity. Fields such as the displacement field $\boldsymbol{u}$ are defined over the entire domain Ω, whereas the restriction of the field to the subdomain Ω_j is denoted $\boldsymbol{u}_j(\boldsymbol{x}, t) \equiv \boldsymbol{u}|_{\Omega_j}$.

The governing equations that describe the linear behavior of the PnC are the homogeneous elastodynamic wave equation, the constitutive equation, and the linear continuity relation, which hold on both parts of the domain:

$$\rho_j \frac{\partial^2 \boldsymbol{u}_j}{\partial t^2} = \nabla \cdot \boldsymbol{\sigma}_j \qquad \text{in } \Omega_j,\ j = \text{i}, \text{h}, \tag{1}$$

$$\boldsymbol{\sigma}_j = \lambda_j \operatorname{tr}\left(\boldsymbol{\varepsilon}_j\right) \boldsymbol{\varepsilon}_j + 2\mu_j \boldsymbol{\varepsilon}_j, \tag{2}$$

$$\boldsymbol{\varepsilon}_j = \frac{1}{2}\left(\nabla \boldsymbol{u}_j + \nabla \boldsymbol{u}_j^{\mathsf{T}}\right), \tag{3}$$

with Bloch–Floquet periodic boundary conditions

$$\boldsymbol{u}\left(\boldsymbol{x} + \boldsymbol{a}_i, t\right) = e^{i(\mathbf{k}\cdot\boldsymbol{a}_i)} \boldsymbol{u}\left(\boldsymbol{x}, t\right) \qquad \text{on } \Gamma_{\text{o}}. \tag{4}$$

In (1) ρ_j is the material density, $\nabla\cdot$ is the divergence operator, $\boldsymbol{u}_j\left(\boldsymbol{x}, t\right)$ is the displacement as a function of position $\boldsymbol{x}$ and time t; similarly, $\boldsymbol{\sigma}_j\left(\boldsymbol{x}, t\right) \equiv \boldsymbol{\sigma}|_{\Omega_j}$ is the Cauchy stress tensor, described by the linearized strain tensor $\boldsymbol{\varepsilon}_j\left(\boldsymbol{x}, t\right) \equiv \boldsymbol{\varepsilon}|_{\Omega_j}$ and Lamé parameters λ_j and ν_j. In (4) $\mathbf{k}$ denotes the wave vector of the traveling wave. In accordance with Bloch–Floquet theory, the displacement field $\boldsymbol{u}$ corresponds to a traveling wave, modulated by some unknown periodic function $\boldsymbol{\Psi}\left(\boldsymbol{x}\right)$ with the same periodicity as the medium:

$$\boldsymbol{u}\left(\boldsymbol{x}, t\right) = e^{i(\mathbf{k}\cdot\boldsymbol{x} - \omega t)} \boldsymbol{\Psi}\left(\boldsymbol{x}\right), \tag{5}$$

where ω is the angular frequency.

In weak form, the elastodynamic wave equation reads: Find $\boldsymbol{u} \in \mathcal{V}^{\star}$ such that

$$\sum_{j=\text{h,i}} \left[\int_{\Omega_j} \rho_j \, \ddot{\boldsymbol{u}}_j \, \boldsymbol{v}_j \, \mathrm{d}\Omega + \int_{\Omega_j} \boldsymbol{\sigma}_j\left(\boldsymbol{u}_j\right) : \boldsymbol{\varepsilon}_j\left(\boldsymbol{v}_j\right) \mathrm{d}\Omega \right] = 0, \qquad \forall \boldsymbol{v} \in \mathcal{V}_0, \tag{6}$$

where $\mathcal{V}^{\star}$ is a *linear variety* that accounts for the non-homogeneous Bloch–Floquet BCs [41], and $\mathcal{V}_0$ is a vector-valued function space on Ω_j, so that

$$\boldsymbol{\mathcal{V}}_0 = \left\{ \boldsymbol{v} \in \left[\mathcal{L}^2\left(\Omega\right)\right]^d,\ \boldsymbol{v}|_{\Omega_i} \in \left[\mathcal{H}^1(\Omega_i)\right]^d,\ \boldsymbol{v}|_{\Gamma_{\text{o}}} = \boldsymbol{0},\ i = \text{h, i} \right\}, \tag{7}$$

where $\mathcal{L}^2\left(\Omega\right)$ is the space of square-integrable functions and $\mathcal{H}^1(\Omega_i)$ is the first-order Sobolev space.

We solve the problem on a domain $\Delta \supseteq \Omega$ that fully encloses the PUC. The discretized domain Δ^h, or *background mesh*, does not necessarily conform to the geometric features of the PUC. To account for the mismatch between the discretization and the PUC's geometry, we choose our weight function and trial solution from the finite-dimensional IGFEM space $\mathcal{S}_e^h \subset \mathcal{V}_0$:

$$\mathcal{S}_e^h = \left\{ \boldsymbol{v}^h\left(\boldsymbol{x}\right) \middle|\ \boldsymbol{v}^h\left(\boldsymbol{x}\right) = \underbrace{\sum_{i\in\iota_h}^{n} N_i(\boldsymbol{x})\boldsymbol{U}_i}_{\text{standard FEM}} + \underbrace{\sum_{i\in\iota_w} s_i \psi_i(\boldsymbol{x})\boldsymbol{\alpha}_i}_{\text{enrichment}}, \quad \boldsymbol{U}_i, \boldsymbol{\alpha}_i \in \mathbb{R}^d \right\}, \tag{8}$$

where ι_h refers to the index set of all original mesh nodes, ι_w is the set of enriched nodes, and s_i refers to a scaling factor that produces well-conditioned system matrices and thus makes the formulation *stable* [51]. The space $\mathcal{S}_e^h$ consists of the standard FEM approximation—the first term with standard Lagrange shape functions N_i and standard DOFs $\boldsymbol{U}_i$—that is augmented with an enriched term that introduces, by means of enrichment functions ψ_i and associated enriched DOFs $\boldsymbol{\alpha}_i$, the required jumps in the gradient of the solution field.

In order to construct the IGFEM enrichment functions, operations on the background mesh using the PUC geometry are required, as illustrated in Fig. 2: new nodes (shown by ● and ○ symbols) are created at intersections of the boundaries (Γ_{o} and Γ_{i}) with edges of elements of the background mesh; the cut elements are subdivided into *integration elements* accordingly, as illustrated with dotted lines. The purpose of these integration elements is fourfold: (i) as their name suggests, the integration elements are used for integration of the elements' local arrays; (ii) the enrichment functions ψ_i are constructed as linear combinations of standard Lagrange shape functions of those integration elements; (iii) the integration elements are used to ensure the field can be displayed correctly after postprocessing; and (iv) the triangular or tetrahedral integration elements are easy to split, thus facilitating a hierarchical implementation when multiple discontinuities cross a single element. Elements that lie completely outside the PUC are removed from the analysis, as are DOFs corresponding to outside nodes (shown with ○

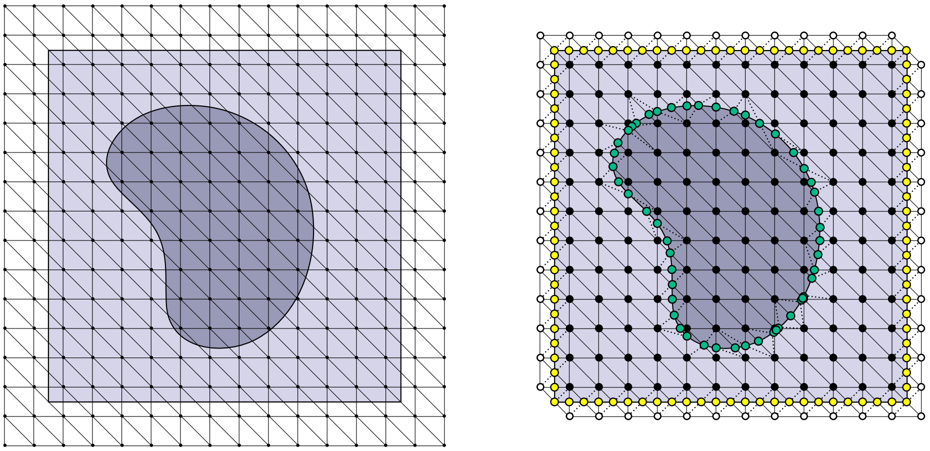

(a) (b)

Fig. 2. Mesh-independent periodic unit cell: (a) The PUC is immersed in a non-matching structured mesh; (b) Enriched nodes are placed along the discontinuities (🟢 and 🟡) and integration elements are created. Elements that lie completely outside the PUC are removed, and nodes outside the PUC (○) are fixed. Bloch–Floquet periodic BCs are applied to enriched nodes on the PUC boundary (🟡).

symbols). In the case that an element is intersected by multiple discontinuities, this procedure can simply be applied hierarchically, as described in detail in [40,51].

Following a Bubnov–Galerkin approach, the discretized system of linear equations, $\boldsymbol{M}\ddot{\boldsymbol{U}} - \boldsymbol{K}\boldsymbol{U} = \boldsymbol{0}$, can now be obtained via standard procedures, with global stiffness and mass matrix, $\boldsymbol{K}$ and $\boldsymbol{M}$, respectively:

$$\boldsymbol{K} = \mathop{\mathbb{A}}_{i} \boldsymbol{k}_i, \quad \boldsymbol{M} = \mathop{\mathbb{A}}_{i} \boldsymbol{m}_i. \tag{9}$$

The finite element assembly operator is here written as $\mathbb{A}$ and $\boldsymbol{k}_i$, $\boldsymbol{m}_i$ denote element local stiffness and mass matrices, respectively, which are obtained by numerical quadrature.

Once $\boldsymbol{K}$ and $\boldsymbol{M}$ are assembled, Bloch–Floquet periodicity is enforced by means of a transformation matrix $\boldsymbol{T}$. This complex matrix contains the complex exponent of the Bloch–Floquet BCs and is therefore a function of the wave vector $\mathbf{k}$. The modified system matrices $\tilde{\boldsymbol{K}}$ and $\tilde{\boldsymbol{M}}$ can be found by pre- and post-multiplying the original matrices with $\boldsymbol{T}$, resulting in complex Hermitian matrices:

$$\begin{aligned} \tilde{\boldsymbol{K}}(\mathbf{k}) &= \boldsymbol{T}(\mathbf{k})^{\mathsf{H}} \boldsymbol{K} \boldsymbol{T}(\mathbf{k}), \\ \tilde{\boldsymbol{M}}(\mathbf{k}) &= \boldsymbol{T}(\mathbf{k})^{\mathsf{H}} \boldsymbol{M} \boldsymbol{T}(\mathbf{k}). \end{aligned} \tag{10}$$

This rectangular transformation matrix $\boldsymbol{T}$ reduces the size of the system of linear equations, as subordinate periodic boundary DOFs are removed (*e.g.*, in contrast to Lagrange multiplier methods, where the system of linear equations is augmented). The costs of these operations are relatively low, as the transformation matrix $\boldsymbol{T}(\mathbf{k})$ is very sparse; for the internal part of the domain it is the identity matrix, and the only off-diagonal terms relate to the boundary DOFs. Due to the sparsity of $\boldsymbol{T}$ as well as $\boldsymbol{K}$ and $\boldsymbol{M}$, these operations can be performed very efficiently. As the boundaries of the PUC are lower-dimensional manifolds (*e.g.*, lines in 2-D and surfaces in 3-D), the cost of these transformations relative to the cost of solving the system reduces with mesh refinement. The dispersion relation—or band structure—is subsequently obtained by performing a series of eigenvalue analyses for a set of wave vectors $\mathbf{k}_j$, defined along the edge of the irreducible Brillouin zone [52]:

$$\left[\tilde{\boldsymbol{K}}(\mathbf{k}_j) - \omega_j^2 \tilde{\boldsymbol{M}}(\mathbf{k}_j)\right] \boldsymbol{V}_j = \boldsymbol{0}, \tag{11}$$

where $\boldsymbol{V}_j$ are complex eigenvectors that represent traveling waves and ω_j are the corresponding eigenfrequencies.

Although IGFEM has not been used in phononic crystal analysis before, it can be readily used to describe the material interfaces within the periodic unit cell. However, when a discontinuity crosses the PUC boundary, or when the PUC itself is non-matching, enriched nodes are subject to Bloch–Floquet periodicity as well, as explained in the next section.

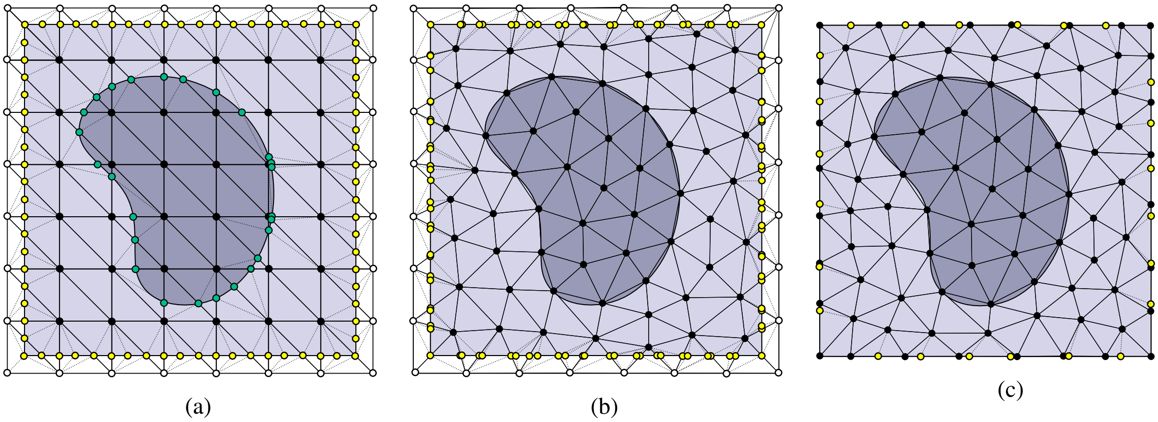

Fig. 3. Cases where boundary nodes are not spaced exactly one lattice vector apart: (a,b) PUCs immersed in a structured (a) and unstructured (b) meshes, where additional enriched nodes are added to properly enforce periodicity; (c) PUC were the mesh conforms to both the inclusion and the outer PUC edge, but the nodes on either side do not coincide, so enriched nodes are added.

2.1. Bloch-Floquet periodicity on enriched nodes

Bloch–Floquet periodic BCs enforce periodicity of the PUC, but allow for a phase difference of the traveling wave between unit cells; they guarantee that the displacements $\boldsymbol{u}$ take the form of a Bloch wave throughout the entire domain, while only operating on the boundaries. As these BCs operate directly on the field $\boldsymbol{u}$, we follow the procedure for Dirichlet BCs on immersed IGFEM edges using multiple point constraints (MPCs), as described by van den Boom et al. [43]. On the boundary nodes of the PUC, Bloch–Floquet periodic boundary conditions are applied as

$$\boldsymbol{u}(\boldsymbol{x}_{\mathrm{s}}) = e^{i\mathbf{k}\cdot\boldsymbol{a}}\boldsymbol{u}(\boldsymbol{x}_{\mathrm{m}}), \tag{12}$$

where $\boldsymbol{u}(\boldsymbol{x}_{\mathrm{m}})$ and $\boldsymbol{u}(\boldsymbol{x}_{\mathrm{s}})$ are displacements corresponding to a main and a subordinate node, respectively. These two nodes are assumed to be separated by exactly one lattice vector $\boldsymbol{a}$, as attempting to apply periodicity to non-matching nodes would result in inaccurate results. In general, enriched nodes are not guaranteed to coincide on either side of the PUC, thus Bloch–Floquet periodicity cannot be enforced directly. In such cases, supplementary enriched nodes can be added to ensure that every enriched boundary node has a counterpart. These extra enriched nodes can easily be accounted for by creating additional integration elements, and as such they do not change the rest of the procedure. Fig. 3 illustrates some situations where the enriched nodes do not coincide exactly. Fig. 3a is similar to Fig. 2 in that it shows a square unit cell immersed in a structured mesh. The difference is that the PUC edges do not lie exactly in the middle of the background elements, so that the intersections with the diagonal element edges do not coincide on either side of the PUC. Other cases where the boundary nodes do not coincide are found in unstructured meshes, regardless of whether the edges are immersed, as in Fig. 3b, or conforming, as in Fig. 3c. In cases where the nodes do not coincide, the full procedure to prescribe the Bloch–Floquet periodic boundary conditions on immersed edges is: (i) Find the intersections between the immersed edges and the background elements; (ii) Create the counterpart of these nodes by adding the lattice vector to the coordinate vector of the node; (iii) Create integration elements taking into account all enriched nodes.

In IGFEM, the enriched DOFs do not directly represent the displacement field at their location because the *partition of unity* property is lost in intersected elements.[4] Instead, the solution also depends on the DOFs of the parent cut element, as given by (8). The solution at the enriched locations can therefore be written for $j = \mathrm{m}, \mathrm{s}$ as:

$$\boldsymbol{u}(\boldsymbol{x}_j) = \sum_{i\in\iota_j} N_i(\boldsymbol{x}_j)\boldsymbol{U}_i + s_j\psi_j(\boldsymbol{x}_j)\boldsymbol{\alpha}_j, \tag{13}$$

---

[4] In IGFEM, enrichment functions $\psi_i(x)$ are added to the standard FEM approximation, breaking the partition of unity. The original shape function N_i do not vanish at the locations of the enriched nodes, and as a result, the displacements at those locations are computed per Eq. (13). However, because enrichment functions vanish at original mesh nodes, the Kronecker-δ property on those nodes is retained and therefore standard DOFs keep their physical meaning.

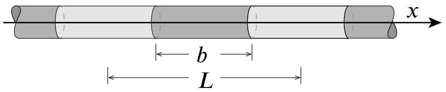

Fig. 4. One-dimensional phononic crystal with PUC of length L.

where the index set $\iota_j \subset \iota_h$ refers to the parent nodes which have a non-zero contribution on the enriched node location $\boldsymbol{x}_j$, and $\psi_j(\boldsymbol{x}_j) = 1$. Expanding (12) in terms of this IGFEM approximation results in an expression from which the subordinate DOFs of the system can be calculated:

$$\boldsymbol{\alpha}_{\mathrm{s}} = \frac{e^{i\mathbf{k}\cdot\boldsymbol{r}}}{s_{\mathrm{s}}\psi_{\mathrm{s}}(\boldsymbol{x}_{\mathrm{s}})}\left[\sum_{i\in\iota_{\mathrm{m}}} N_i(\boldsymbol{x}_{\mathrm{m}})\boldsymbol{U}_i + s_{\mathrm{m}}\psi_{\mathrm{m}}(\boldsymbol{x}_{\mathrm{m}})\boldsymbol{\alpha}_{\mathrm{m}}\right] - \frac{1}{s_{\mathrm{s}}\psi_{\mathrm{s}}(\boldsymbol{x}_{\mathrm{s}})}\sum_{i\in\iota_{\mathrm{s}}} N_i(\boldsymbol{x}_{\mathrm{s}})\boldsymbol{U}_i. \tag{14}$$

Writing such a constraint equation for every subordinate node results in a system of equations, that can be written in the form:

$$\begin{bmatrix}\boldsymbol{U}\\ \boldsymbol{\alpha}\end{bmatrix} = \boldsymbol{T}\begin{bmatrix}\tilde{\boldsymbol{U}}\\ \tilde{\boldsymbol{\alpha}}\end{bmatrix}, \tag{15}$$

where $\boldsymbol{T}$ is a complex-valued transformation matrix that is a function of wave vector $\mathbf{k}$, and that maps between the free system $\begin{bmatrix}\boldsymbol{U} & \boldsymbol{\alpha}\end{bmatrix}^{\mathsf{T}}$ and the constrained system $\begin{bmatrix}\tilde{\boldsymbol{U}} & \tilde{\boldsymbol{\alpha}}\end{bmatrix}^{\mathsf{T}}$. The system matrices can now be modified as described in Eq. (10). A one-dimensional example on the construction of $\boldsymbol{T}$ is given in the Appendix.

In cases where the parent elements of the outer edges of the PUC are intersected by multiple discontinuities, *e.g.*, when the immersed inclusion crosses the PUC edge, a hierarchical implementation of the multiple point constraint is required. This implementation follows naturally from the HIFEM approximation, and is described for Dirichlet boundary conditions by van den Boom et al. [43].

3. Numerical results

3.1. 1-D phononic crystal

Consider in Fig. 4 a 1-D phononic crystal composed of two materials of dissimilar properties. A PUC of length $L \equiv \|a_1\|$ can be defined such that its boundaries lie on the host and the other material outlines an inclusion of length b. The materials used are polycarbonate and lead for the host and inclusion, respectively. Polycarbonate (lead) has an elasticity modulus $E_1 = 2.3\,\mathrm{GPa}$ ($E_2 = 16\,\mathrm{GPa}$) and density $\rho_1 = 1200\ \mathrm{kg/m^3}$ ($\rho_2 = 11\,340\ \mathrm{kg/m^3}$). This phononic crystal has a total unit cell length $L = 25\,\mathrm{mm}$, with an inclusion of length $b = 14\,\mathrm{mm}$. Therefore, the length of the two sections are $l_{\mathrm{h}} = 11\,\mathrm{mm}$ and $l_{\mathrm{i}} = 14\,\mathrm{mm}$, respectively.

Following [53] for the analytic solution, we scale the lengths by l_{h} and time by $l_{\mathrm{h}}/c_{\mathrm{h}}$, where c_{h} is the wave speed in the host material. This problem can then be described by the non-dimensionalized 1-D wave equation on both material domains ($i = \mathrm{h}, \mathrm{i}$):

$$\frac{\partial^2 u_i(x,t)}{\partial x^2} = \frac{1}{c_i/c_{\mathrm{h}}}\frac{\partial^2 u_i(x,t)}{\partial t^2}, \tag{16}$$

with the wave speeds

$$c_i = \sqrt{E_i/\rho_i}, \tag{17}$$

interface conditions

$$u_{\mathrm{h}}(1,t) = u_{\mathrm{i}}(1,t), \tag{18}$$

$$u_{\mathrm{h}}'(1,t) = \frac{E_2}{E_1}u_{\mathrm{i}}'(1,t), \tag{19}$$

Bloch–Floquet periodic boundary conditions

$$u_{\mathrm{h}}(0,t) = u_{\mathrm{i}}(1+\frac{L_{\mathrm{i}}}{L_{\mathrm{h}}},t)\,\lambda, \tag{20}$$

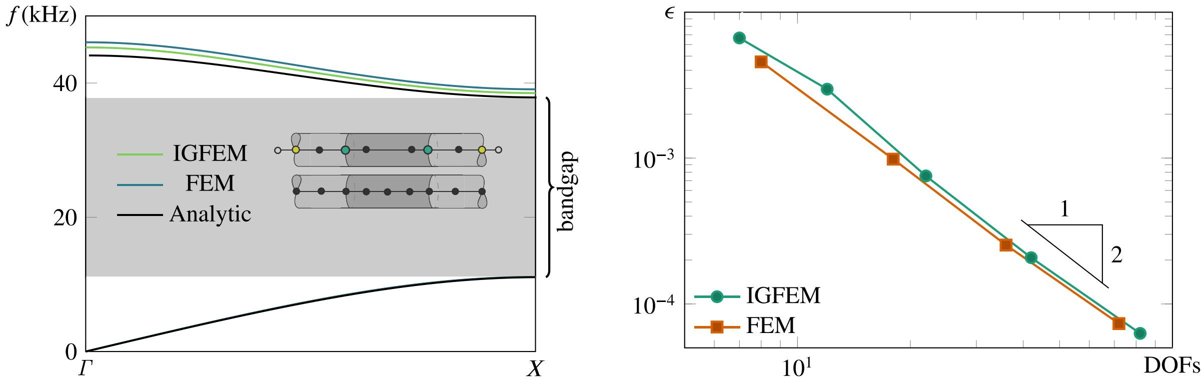

(a) (b)

Fig. 5. (a) Dispersion curve (band structure) and bandgap for the 1-D phononic crystal, where the IGFEM result on a 5-element background mesh is compared to a matching mesh with a comparable number of DOFs; (b) Mesh convergence for the relative error in the first two bands given by Eq. (24).

$$u'_{\mathrm{h}}(0,t) = \frac{E_{\mathrm{i}}}{E_{\mathrm{h}}} u'_2\left(1 + \frac{L_{\mathrm{i}}}{L_{\mathrm{h}}}, t\right) \lambda, \tag{21}$$

and with the propagation constant $\lambda = e^{ikL}$. A non-trivial solution to the system of equations can be found if λ is a solution to the characteristic equation

$$\lambda^2 + q(\hat{\omega})\lambda + 1 = 0, \tag{22}$$

with

$$q(\hat{\omega}) = -2\cos(\hat{\omega})\cos(\tau\hat{\omega}) + \left(\kappa + \frac{1}{\kappa}\right)\sin(\hat{\omega})\sin(\tau\hat{\omega}), \tag{23}$$

where $\tau = l_{\mathrm{i}} c_{\mathrm{h}} / l_{\mathrm{h}} c_{\mathrm{i}}$ is the ratio of propagation times, and $\kappa = E_{\mathrm{i}} c_{\mathrm{h}} / E_{\mathrm{h}} c_{\mathrm{i}}$ is the ratio of impedances of the two materials. Looping over $\hat{\omega}$ and solving for λ, the analytic solution can be computed.

The numerical results are obtained using two different approaches: (i) standard FEM using matching meshes; (ii) IGFEM using meshes that do not match to the PUC edges nor to the material interfaces. We define the error with respect to the analytic solution as

$$\epsilon = \sqrt{\frac{1}{|K|N} \frac{\sum_{\mathrm{k}\in K} \sum_n (\omega_{\mathrm{k},n} - \hat{\omega}_{\mathrm{k},n})^2}{\sum_{\mathrm{k}\in K} \sum_n \hat{\omega}^2_{\mathrm{k},n}}} \qquad n = 1, 2, \ldots, N, \tag{24}$$

where K is the set of wave numbers in the Brillouin zone, $K = \{\Gamma, \ldots, X\}$, with cardinality $|K|$, $\hat{\omega}_{\mathrm{k},n}$ denotes the nth analytic frequency for a given wave number k and $\omega_{\mathrm{k},n}$ is the numerical counterpart. In other words, Eq. (24) is the relative error in the L^2-norm of the first N bands evaluated at $|K|$ wave numbers.

The first two bands of the band structure are shown in Fig. 5a for the analytical solution and the two numerical results that were obtained on a fixed mesh size with meshes composed of 5 elements. Both FEM and IGFEM give more accurate results for lower frequencies, so more deviation from the analytic result is expected in the higher bands. Fig. 5b considers mesh refinement and shows the convergence for the error (24) as a function of the number of DOFs, with $N = 5$ and $|K| = 100$. It is shown that IGFEM has the same rate of convergence as the standard FEM on matching meshes.

3.2. 2-D uniform material

To investigate the performance of the enriched boundary conditions in 2-D, we consider the velocity of pressure and shear waves through a uniform polycarbonate slab, with a Poisson ratio $\nu = 0.37$ and, as in the previous example, $E = 2.3$ GPa and $\rho = 1200$ kg/m^3. It should be noted that this is not a PnC, and as such, no dispersion is

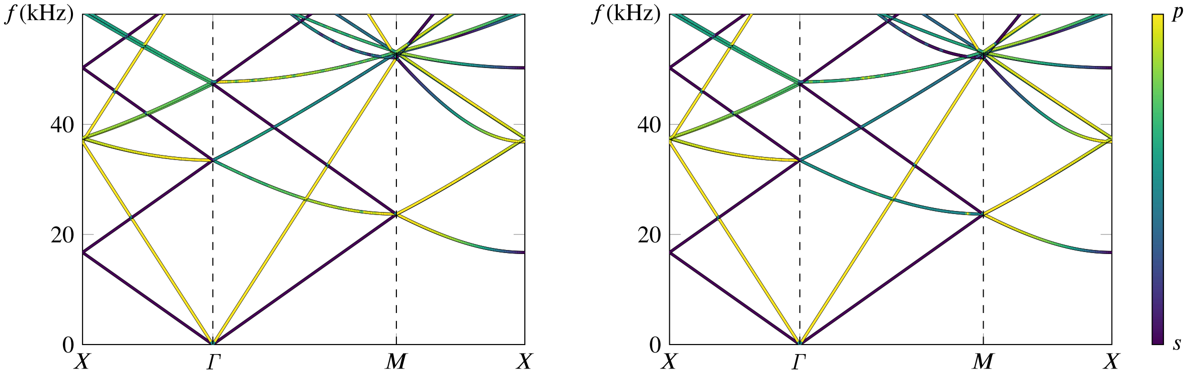

(a)

(b)

Fig. 6. Band structure for a PUC of uniform polycarbonate, obtained on a 60 × 60 matching mesh (a), and on a 60 × 60 non-matching mesh with enriched Bloch–Floquet boundary conditions (b). The nature of each wave in the uniform material is investigated in more detail: the color of each line signifies whether the wave is an s-wave (blue), a p-wave (yellow), or a combination thereof. Both matching and non-matching meshes recover the same wave types for each band. (For interpretation of the references to color in this figure legend, the reader is referred to the web version of this article.)

expected. This material is analyzed using a square PUC with a side length $L = 0.025\,\text{m}$, so that the lattice vectors $\boldsymbol{a}_i$ and reciprocal lattice vectors $\boldsymbol{b}_i$ are given by

$$\boldsymbol{a}_1 = \begin{bmatrix} 0.025 \\ 0 \end{bmatrix} \text{m}, \ \boldsymbol{a}_2 = \begin{bmatrix} 0 \\ 0.025 \end{bmatrix} \text{m}, \ \boldsymbol{b}_1 = \begin{bmatrix} 251.33 \\ 0 \end{bmatrix} \text{m}^{-1}, \ \boldsymbol{b}_2 = \begin{bmatrix} 0 \\ 251.33 \end{bmatrix} \text{m}^{-1}. \tag{25}$$

The vertices of the irreducible Brillouin zone are therefore located at $\Gamma = \begin{bmatrix} 0 & 0 \end{bmatrix}^\intercal \text{m}^{-1}$, $X = \begin{bmatrix} 125.66 & 0 \end{bmatrix}^\intercal \text{m}^{-1}$ and $M = \begin{bmatrix} 125.66 & 125.66 \end{bmatrix}^\intercal \text{m}^{-1}$. The PUC is analyzed using standard FEM and IGFEM using a 60 × 60 structured mesh with triangular elements for both cases, and results are reported in Fig. 6. The nature of each band, which is found by projecting the normalized displacements in the vibration mode onto the wave vector using a dot product and averaging the nodal results, is plotted in Figs. 6a and 6b, for standard FEM and IGFEM, respectively. Blue refers to a pure shear wave and yellow refers to a pure pressure wave. It is clear that both methods recover the same wave types for each band.

The velocities of shear and pressure waves are now recovered numerically as

$$v_s = \frac{2\pi f_s}{\|\mathbf{k}\|} \ \text{and} \ v_p = \frac{2\pi f_p}{\|\mathbf{k}\|}. \tag{26}$$

The numerical wave velocities, computed using IGFEM (or FEM) as $v_s = 836.53$ m/s and $v_p = 1841.53$ m/s, are in close agreement with the exact velocities,

$$\hat{v}_s = \sqrt{\frac{G}{\rho}} = 836.37 \text{ m s}^{-1} \ \text{and} \ \hat{v}_p = \sqrt{\frac{M}{\rho}} = 1841.18 \text{ m s}^{-1}, \tag{27}$$

where the shear modulus G and pressure wave modulus M are given, respectively, by

$$G = \frac{E}{2\,(1-2\nu)} \ \text{and} \ M = \frac{E\,(1-\nu)}{(1+\nu)\,(1-2\nu)}. \tag{28}$$

To study the convergence of the wave velocities, we define an error norm for the shear and pressure waves:

$$\epsilon_s = \sqrt{\frac{\left(v_s - \hat{v}_s\right)^2}{\hat{v}_s^2}}\ , \ \epsilon_p = \sqrt{\frac{\left(v_p - \hat{v}_p\right)^2}{\hat{v}_p^2}}. \tag{29}$$

In the results of Fig. 7 it is shown that IGFEM and standard FEM converge towards the exact solution at the same terminal convergence rate. Furthermore, the absolute value of the error is similar for FEM and IGFEM. Therefore, it can be concluded that the enriched boundary conditions do not influence the solution in 2-D.

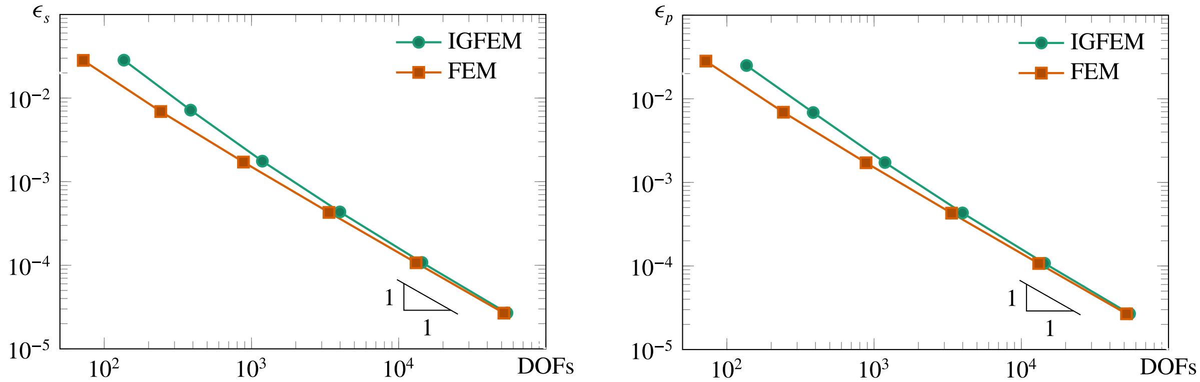

(a) (b)

Fig. 7. Convergence of the shear wave velocity (a) and pressure wave velocity (b) for a uniform material. Both the shear wave velocity and the pressure wave velocity converge at the same rate for standard FEM and IGFEM.

3.3. 2-D phononic crystal with a circular inclusion

A 2-D phononic crystal containing a circular inclusion of radius r in a square lattice is now analyzed. A PUC of size $L \times L$ can be defined, as illustrated in Fig. 8. The same materials as for the 1-D phononic crystal are used for the host and inclusion; polycarbonate and lead ($E_1 = 2.3\,\text{GPa}$, $E_2 = 16\,\text{GPa}$, $\nu_1 = 0.37$, $\nu_2 = 0.44$, $\rho_1 = 1200\ \text{kg/m}^3$, $\rho_2 = 11\,340\ \text{kg/m}^3$). The dimensions of this PnC are $L = 25\,\text{mm}$ and $r = 7\,\text{mm}$. The lattice vectors and reciprocal lattice vectors for this problem are the same as in the previous example, as the unit cell is of the same dimensions. Therefore, the locations of the Brillouin zone vertices are also the same, located at $\Gamma = \begin{bmatrix} 0 & 0 \end{bmatrix}^\intercal \text{m}^{-1}$, $X = \begin{bmatrix} 125.66 & 0 \end{bmatrix}^\intercal \text{m}^{-1}$ and $M = \begin{bmatrix} 125.66 & 125.66 \end{bmatrix}^\intercal \text{m}^{-1}$.

The numerical results, obtained using IGFEM on different mesh sizes, are compared to the results obtained using standard FEM on a very fine (overkill) matching mesh, which we will regard to be the correct result. From the band structure in Fig. 8c, it can be seen that a bandgap opens in the range 18 kHz to 28 kHz. Some propagation bands appear in the bandgap for very coarse meshes, but with mesh refinement, the bandgap converges towards that of the reference matching mesh. The error for each band n with respect to the reference solution is defined by

$$\epsilon_n = \sqrt{\frac{1}{|K|} \frac{\sum_{\mathbf{k}\in K} (\omega_{\mathbf{k},n} - \omega^*_{\mathbf{k},n})^2}{\sum_{\mathbf{k}} \omega^{*2}_{\mathbf{k},n}}}, \tag{30}$$

where K defines a set of wave vectors $\mathbf{k}$ along the irreducible Brillouin zone ($X \to \Gamma \to M \to X$). Furthermore, an error norm is defined for the frequencies that define the bandgap between the third and the fourth propagation bands:

$$\epsilon_{\text{low}} = \sqrt{\frac{\left(\max(\omega_{\mathbf{k},3}) - \max(\omega^*_{\mathbf{k},3})\right)^2}{\max(\omega^*_{\mathbf{k},3})^2}} \quad \text{and} \quad \epsilon_{\text{high}} = \sqrt{\frac{\left(\min(\omega_{\mathbf{k},4}) - \min(\omega^*_{\mathbf{k},4})\right)^2}{\min(\omega^*_{\mathbf{k},4})^2}}. \tag{31}$$

The convergence of the first 5 bands is shown in Fig. 9a. The error increases slightly for the higher bands, which is to be expected in eigenvalue analysis because the higher frequencies correspond to shorter wave lengths which are not captured accurately by the relatively coarse discretizations. Nonetheless, all bands converge at the same rate. In Fig. 9b it is shown that the frequencies that define the bandgap converge at a slightly higher rate (1.5).

The motion of a wave traveling between Γ and X ($\mathbf{k} = \begin{bmatrix} 62.83 & 62.83 \end{bmatrix}^\intercal \text{m}^{-1}$) on the first propagation band, obtained from a coarse IGFEM mesh and a fine FEM mesh, are now compared. Fig. 10a shows a snapshot of a traveling wave for the very fine matching mesh, while Figs. 10b and 10c show the same wave at the same time on a non-matching mesh defined over a 10×10 grid. The same mode is indeed resolved on both meshes.

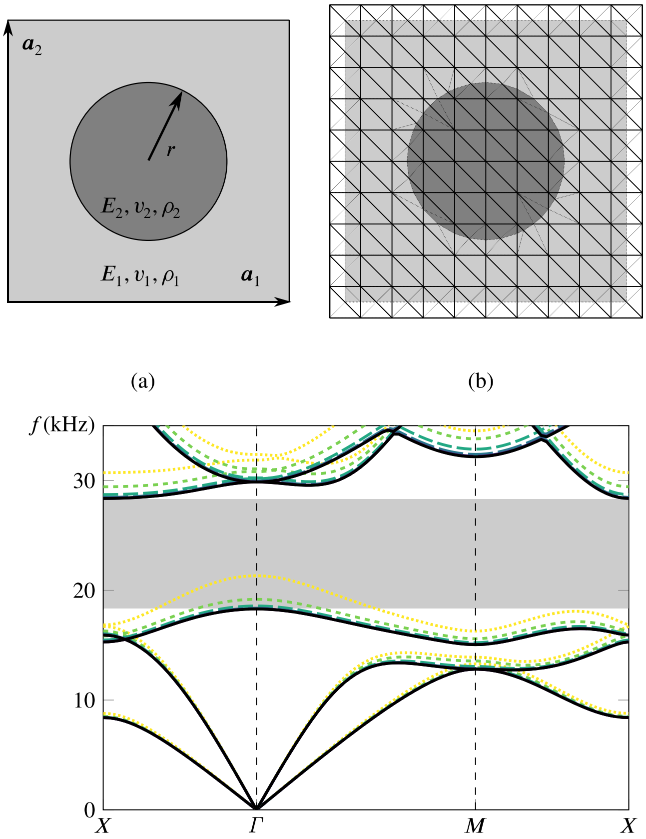

(a) (b)

(c)

Fig. 8. (a) Schematic of a square PUC with lattice vectors $\boldsymbol{a}_1$ and $\boldsymbol{a}_2$ and a circular inclusion of radius r; (b) the PUC is immersed in a 10 × 10 non-matching structured mesh; (c) Band structure for a square PUC with a circular inclusion, obtained by multiple non-matching meshes consisting of 5 × 5 × 2 (┈┈┈), 10 × 10 × 2 (╌╌╌), 20 × 20 × 2 (━ ━), 40 × 40 × 2 (━━ ━), 80 × 80 × 2 (━━━), and 160 × 160 × 2 (━━━) triangular elements and a very fine matching mesh (━━━). The bandgap is plotted for the finest matching mesh. Clearly, a coarse representation of a non-matching mesh results in propagation bands inside the gap. However, the bandgap converges with mesh refinement.

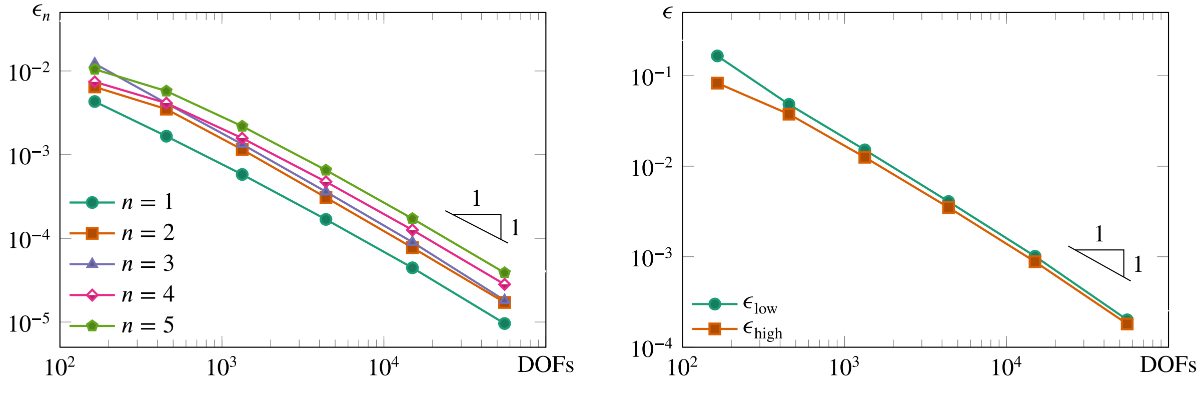

(a) (b)

Fig. 9. Convergence for the PnC with a circular inclusion in a square lattice. In (a), the error for the first five propagation bands as defined in Eq (30) is shown to have the same rate of convergence. In (b) the convergence of the error defined in Eq. (31) is shown for the frequencies that define the bandgap.

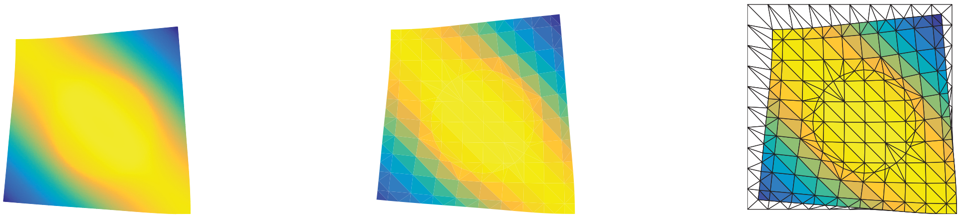
(a) (b) (c)

Fig. 10. Snapshot of a traveling wave on the lowest band between Γ and M on (a) a fine matching mesh; (b) a 10 × 10 non-matching structured mesh; the non-matching mesh is also shown in (c). The same mode shapes are obtained for both analyses.

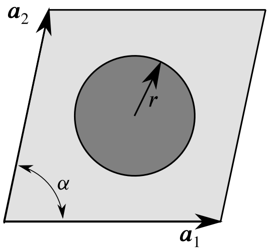

Fig. 11. General periodic unit cell for the phononic crystal with a varying lattice: the angle α between lattice vectors $\boldsymbol{a}_1$ and $\boldsymbol{a}_2$ is varied while the inclusion with radius r is kept the same.

Table 1
Lattice vectors $\boldsymbol{a}_i$ and reciprocal lattice vectors $\boldsymbol{b}_i$ for the different lattice angles α that were analyzed on the same structured meshes.

Lattice angle α	Lattice vectors		Reciprocal lattice vectors	
	$\boldsymbol{a}_1$ (m)	$\boldsymbol{a}_2$ (m)	$\boldsymbol{b}_1$ (m^{-1})	$\boldsymbol{b}_2$ (m^{-1})
60° (Triangular lattice)	$[0.027 \quad 0.000]^{\mathsf{T}}$	$[0.013 \quad 0.023]^{\mathsf{T}}$	$[233.89 \quad -135.03]^{\mathsf{T}}$	$[0.00 \quad 270.07]^{\mathsf{T}}$
70° (Rhombic lattice)	$[0.026 \quad 0.000]^{\mathsf{T}}$	$[0.009 \quad 0.024]^{\mathsf{T}}$	$[243.63 \quad -88.67]^{\mathsf{T}}$	$[0.00 \quad 259.27]^{\mathsf{T}}$
80° (Rhombic lattice)	$[0.025 \quad 0.000]^{\mathsf{T}}$	$[0.004 \quad 0.024]^{\mathsf{T}}$	$[249.41 \quad -43.98]^{\mathsf{T}}$	$[0.00 \quad 253.26]^{\mathsf{T}}$
90° (Square lattice)	$[0.025 \quad 0.000]^{\mathsf{T}}$	$[0.000 \quad 0.025]^{\mathsf{T}}$	$[251.33 \quad 0.00]^{\mathsf{T}}$	$[0.00 \quad 251.33]^{\mathsf{T}}$

3.4. 2-D phononic crystal with a varying lattice

In previous examples, the combinations of PUC and background mesh were chosen such that enriched nodes, placed at intersections of the background elements with the PUC edge, were separated by exactly one lattice vector. This means that only certain configurations of PnCs could be analyzed within a given mesh. However, to achieve true mesh-geometry decoupling this requirement is now removed. Additional enriched DOFs are placed on either side of the PUC to ensure that each enriched node has a periodic counterpart. In this numerical example, phononic crystals with different lattices, with a variable angle α between both lattice vectors, are analyzed on the same square structured mesh, for which the general PUC is illustrated in Fig. 11. The different PnCs, with a circular inclusion ($r = 7$ mm), are chosen such that the volume fraction of the inclusion versus the host material is the same ($\phi = 0.2463$). Furthermore, for each phononic crystal, the magnitude of both lattice vectors are chosen to be the same ($\|\boldsymbol{a}_1\| = \|\boldsymbol{a}_2\|$), such that the lattices are triangular ($\alpha = 60°$), square ($\alpha = 90°$), or rhombic ($\alpha = 70°$ and $\alpha = 80°$). The lattice vectors that were used for the four cases, and their corresponding reciprocal lattice vectors, are given in Table 1.

The material properties of the inclusion and host are the same as in previous examples. In the discretization of these PUCs, extra enriched nodes are placed along the PUC edge, such that all enrichments are spaced exactly one lattice vector apart. Only then can Bloch–Floquet periodic boundary conditions be applied as described in Section 2.1. Fig. 12 illustrates the coarsest integration mesh for each periodic unit cell.

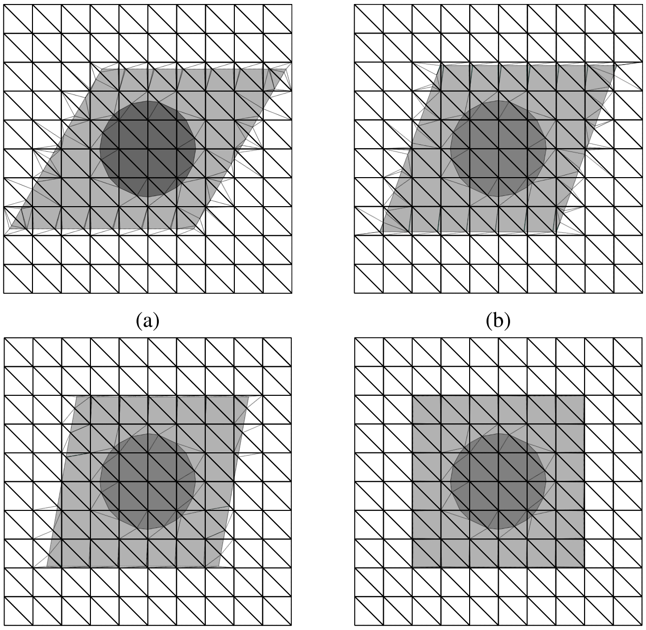

(a) (b) (c) (d)

Fig. 12. Integration meshes for the four periodic unit cells, analyzed on the coarsest structured mesh defined on a 10 × 10 grid.

Each layout is analyzed on a square grid of 10 × 10 × 2, 20 × 20 × 2, 40 × 40 × 2, and 80 × 80 × 2 triangular elements, and on a fine matching mesh. Fig. 13 summarizes the results of the different PnCs. On the left, the PUC and corresponding irreducible Brillouin zone are illustrated. The middle figures show the band structures for the different PnCs, computed on different mesh sizes. The results given on the right in Fig. 13 show that the convergence rates of these dispersion bands are the same as those in previous examples. In Fig. 14, snapshots of waves are given for the same wave vector in different phononic crystals: Fig. 14(a-d) correspond to the Brillouin zone vertex M of the triangular lattice, and Fig. 14(e-f) correspond to the Brillouin zone vertex M of the square lattice. For the rhombic lattices, neither wave vector corresponds to a symmetry point. Therefore, Figs. 14a and 14h correspond to standing waves, whereas the other figures represent traveling waves. This is confirmed by the fact that the modes in Figs. 14a and 14h are symmetric, and the rest are not.

3.5. 3-D phononic crystal

To demonstrate the method in 3-D, we analyze a cubic PUC with a popcorn-shaped inclusion. This geometry is described by the function

$$\phi\left(\boldsymbol{x}\right) = \sqrt{\|\boldsymbol{x}\|} - r - \sum_{k=0}^{11} A \exp\left[-\frac{\left\|\boldsymbol{x} - \boldsymbol{x}^{(k)}\right\|}{\varsigma^{2}}\right], \tag{32}$$

where $r = 0.6$, $\varsigma = 0.2$, $A = 4$, and

$$\boldsymbol{x}^{(k)} = \begin{cases} \frac{r}{\sqrt{5}}\begin{bmatrix}2\cos\left(\frac{2k\pi}{5}\right) & 2\sin\left(\frac{2k\pi}{5}\right) & 1\end{bmatrix}^{\mathsf{T}} & \text{for } 0 \leq k \leq 4, \\ \frac{r}{\sqrt{5}}\begin{bmatrix}2\cos\left(\frac{(2(k-5)-1)\pi}{5}\right) & 2\sin\left(\frac{(2(k-5)-1)\pi}{5}\right) & -1\end{bmatrix}^{\mathsf{T}} & \text{for } 5 \leq k \leq 9, \\ \begin{bmatrix}0 & 0 & r\end{bmatrix}^{\mathsf{T}} & \text{for } k = 10, \\ \begin{bmatrix}0 & 0 & -r\end{bmatrix}^{\mathsf{T}} & \text{for } k = 11. \end{cases} \tag{33}$$

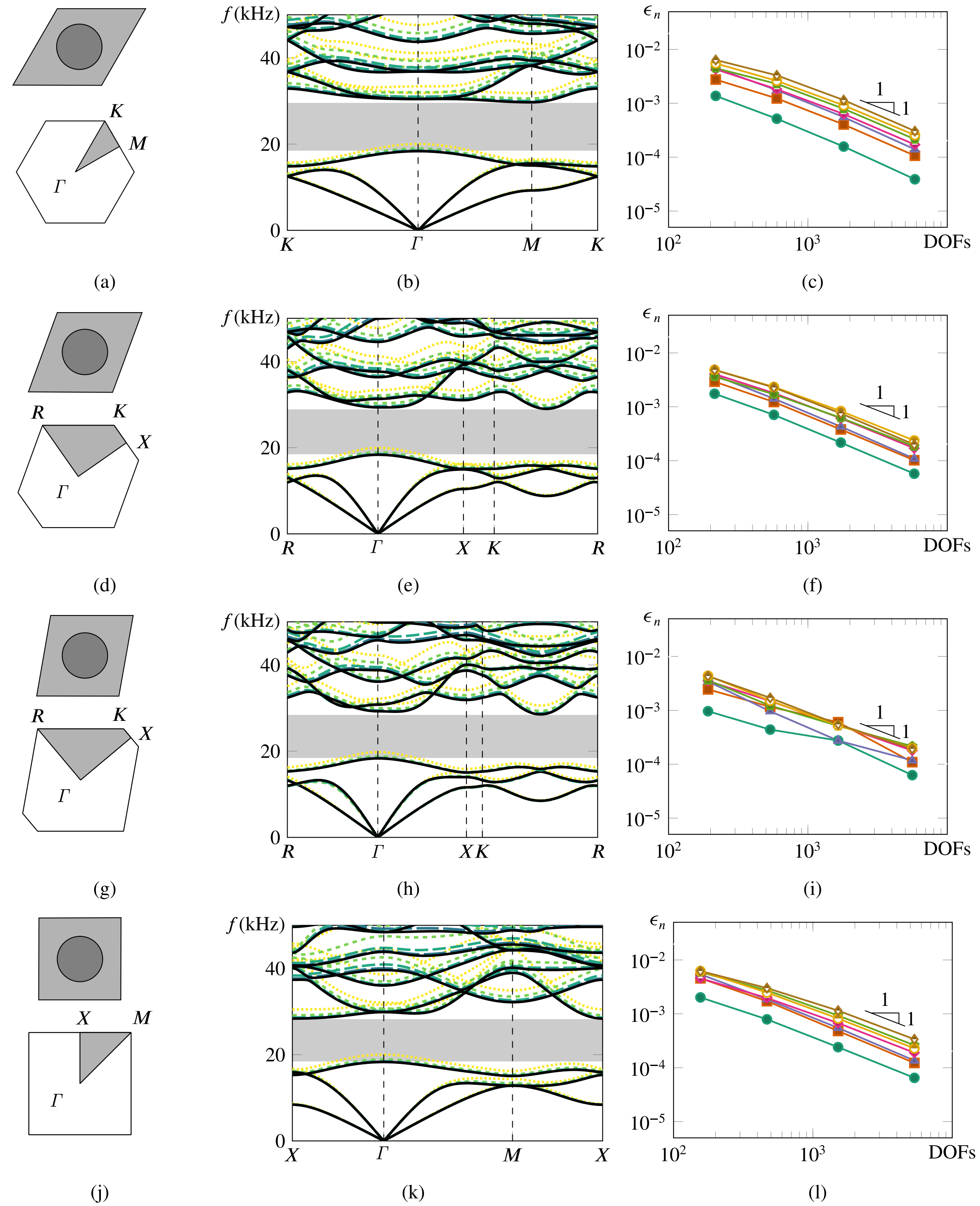

Fig. 13. Phononic crystals with the same volume fractions but with different lattice types (*i.e.*, with PUCs of different shapes) are analyzed on structured meshes. In (a), (d), (g), and (j) periodic unit cells and their corresponding (irreducible) Brillouin zones are shown. Their corresponding dispersion curves are shown in (b), (e), (h), and (k), where results of structured meshes consisting of 10 × 10 × 2 (┈┈┈), 20 × 20 × 2 (╌╌╌), 40 × 40 × 2 (━ ━), 80 × 80 × 2 (━━ ━) triangular elements, and a matching mesh (━━━) are compared. The convergence rates of the first seven bands, as defined in (30), are plotted in (c), (f), (i), and (l).

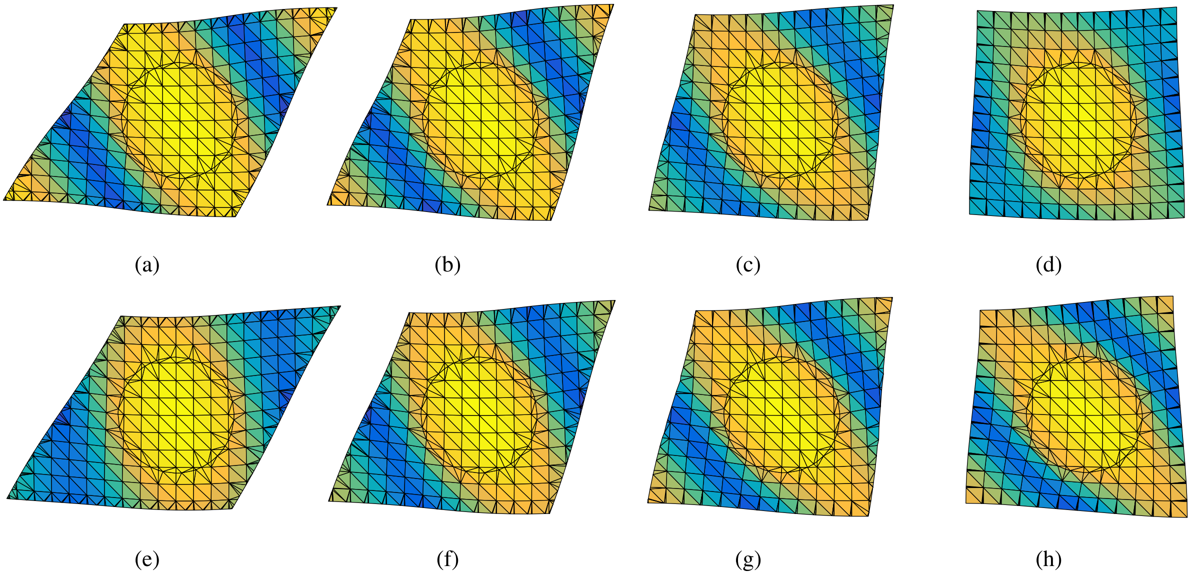

Fig. 14. Snapshots of a wave with wave vector $[116.94, 67.52]^{\mathsf{T}}$ m^{-1}, *i.e.*, M for the triangular lattice (a)–(d), and with wave vector $[125.67, 125.67]^{\mathsf{T}}$ m^{-1}, *i.e.*, M for the square lattice (e)–(h). Figures (a) and (h) correspond to standing waves, whereas the others to traveling waves. This illustrates the different behavior of the same wave vector in different periodic media.

The PUC has volume $L \times L \times L$, where $L = 25\,\mathrm{mm}$, and is immersed in a larger background mesh. The PUC is illustrated in Fig. 15a. As constituent materials, we again use polycarbonate (lead) for the host (inclusion). The vertices of the 3-D irreducible zone are located at $\Gamma = \begin{bmatrix}0 & 0 & 0\end{bmatrix}^{\mathsf{T}}\,\mathrm{m}^{-1}$, $X = \begin{bmatrix}125.66 & 0 & 0\end{bmatrix}^{\mathsf{T}}\,\mathrm{m}^{-1}$, $M = \begin{bmatrix}125.66 & 125.66 & 0\end{bmatrix}^{\mathsf{T}}\,\mathrm{m}^{-1}$ and $R = \begin{bmatrix}125.66 & 125.66 & 125.66\end{bmatrix}^{\mathsf{T}}\,\mathrm{m}^{-1}$. The resulting band structure is obtained on non-matching tetrahedral meshes defined on $6 \times 6 \times 6$, $8 \times 8 \times 8$, $10 \times 10 \times 10$ and $12 \times 12 \times 12$ grids (with 6 tetrahedra per cubic unit in the grid), and on a matching mesh composed of 33 610 tetrahedral elements. Fig. 16 illustrates the results, where it is shown that even on coarse meshes, reasonable approximations can be made on non-matching meshes in 3-D.

4. Summary and conclusions

In this paper we achieved, for the first time, full decoupling of mesh and geometry in the analysis of phononic crystals in 1-D, 2-D, and 3-D by means of immersed analysis of periodic unit cells using the Interface-enriched Generalized Finite Element Method. Both the inclusion and the outer edges of the PUC are allowed to be defined independently from the background mesh, either explicitly (by line segments) or implicitly (by means of a level set function). Bloch–Floquet periodic boundary conditions are applied in a strong manner using multiple point constraints, reminiscent of the strong application of Dirichlet boundary conditions proposed recently in [43]. As the IGFEM operations are restricted to lower-dimensional manifolds (*i.e.*, the material interfaces and PUC boundaries), they do not dominate the computational costs for sufficiently refined meshes; the computational costs are dominated by solving the eigenvalue problem. The resulting formulation provides considerable flexibility in the analysis of phononic crystals with varying inclusions and/or lattices.

The method's convergence properties were compared to standard FEM. This was done by means of two numerical examples: a 1-D phononic crystal, where the methods were compared against an analytic solution proposed in [19], and a 2-D uniform material, where the numerical band structures were used to compute velocities for shear and pressure waves that were compared to analytical velocities. In both 1-D and 2-D examples, the convergence rates of IGFEM and standard FEM were found to be the same. Therefore, the results obtained on a very fine matching mesh were used as reference solution for the following examples.

Several 2-D phononic crystals were analyzed. First, the strong enforcement of Bloch–Floquet periodic boundary conditions on non-matching edges was demonstrated on carefully chosen combinations of PUC and background

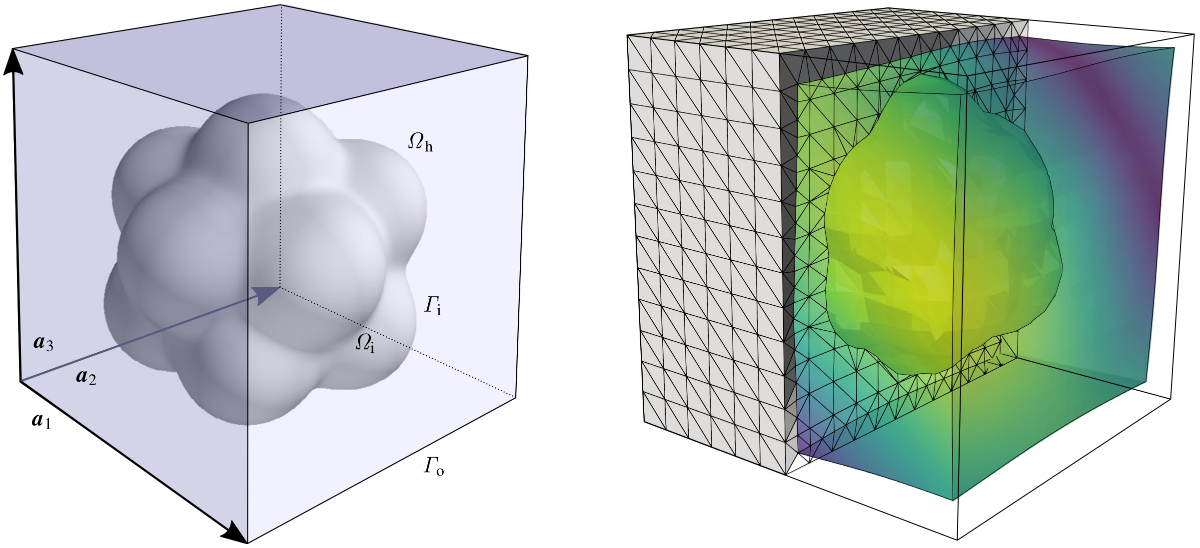

(a) (b)

Fig. 15. Three dimensional phononic crystal: (a) Schematic of the cubic PUC with lattice vectors $\boldsymbol{a}_1$, $\boldsymbol{a}_2$ and $\boldsymbol{a}_3$ and a popcorn-shaped inclusion. The host material is polycarbonate, and the inclusion is made of lead; (b) The deformed PUC is completely immersed in a non-matching background mesh. In this snapshot, a traveling wave in $\Gamma \to R$ is illustrated.

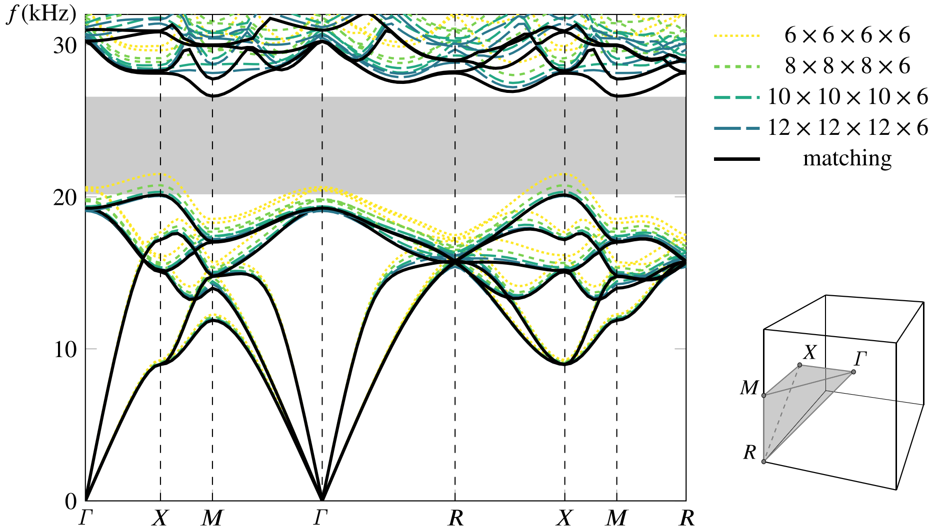

Fig. 16. Dispersion curve for a cubic PUC with a popcorn-shaped inclusion, obtained by multiple non-matching meshes and a matching mesh. The bandgap is plotted for the matching mesh. In different colors, IGFEM solutions for different mesh sizes are shown. The irreducible Brillouin zone of the cubic lattice is plotted to the right. It is found that even for coarse meshes, a reasonable prediction of the bandstructure can be obtained. (For interpretation of the references to color in this figure legend, the reader is referred to the web version of this article.)

mesh (Section 3.2); they were chosen such that enriched nodes on either side of the PUC matched up exactly, so that no extra steps were required for the enforcement of BCs. In the example of Section 3.4, this requirement was released, and 2-D phononic crystals of different non-matching lattice shapes were analyzed. To that end, extra enriched nodes were added along the PUC edges to ensure periodicity could be enforced properly. In both cases, the results were shown to converge to those of the fine matching mesh at the same rate that was previously found. Lastly, a 3-D phononic crystal with a popcorn-shaped inclusion was analyzed. In the examples shown in this paper, the

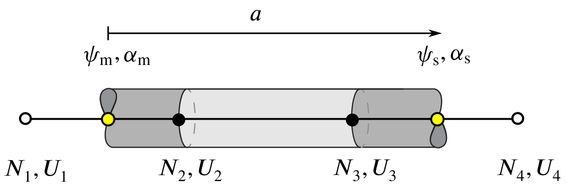

Fig. 17. One-dimensional mesh that is non-matching to the PnC on the outer boundaries for the demonstration of the construction of the $\boldsymbol{T}$ matrix.

inclusions and PUC boundaries never intersect the same background element. Through the use of HIFEM [40], it is also possible to analyze unit cells where the inclusion crosses the PUC boundary. However, the boundary conditions would also need to be implemented hierarchically, as described for Dirichlet boundary conditions elsewhere [43].

As other enriched methods, IGFEM also has a number of drawbacks. For example, as shown in [54,55], IGFEM overestimates stresses in integration elements with bad aspect ratios. Although it has been shown that this effect is less prominent near Dirichlet boundaries [43], and in the context of DE-FEM near traction-free cracks [42], the approximation of stresses in elements with bad aspect ratios is still an open research question. Furthermore, as in standard FEM, the higher bands are approximated less accurately. Higher order interpolation functions and enrichment functions could be investigated to mitigate this drawback.

To the best of our knowledge, this is the first work in which complete decoupling of the mesh and geometry in the analysis of phononic crystals with the same accuracy as that of standard FEM with matching meshes is demonstrated. The advantage of decoupling the mesh from the geometry is most apparent in cases where the geometry of the PUC is not known *a priori*, such as during the design or optimization of the phononic crystal PUC. Using this method, a range of phononic crystals can readily be analyzed without the need for remeshing, and the immersed optimization of phononic crystals is a matter of computing sensitivities and including an optimization loop. As the geometry of the inclusion may be defined implicitly by a level set, the level-set based enriched topology optimization introduced in [49] may be employed. In fact, the topology optimization of PnCs using IGFEM is the subject of an incoming publication. Following Veres et al. [12] it is also possible to extend the enriched method in a $\mathbf{k}(\omega)$-formulation, which can be used to also obtain the evanescent waves. In this method, dynamic condensation is used to reduce the problem to its boundary nodes. The properties of the wave vectors along the irreducible Brillouin zone are then used to write the problem as palindromic quadratic and quartic eigenvalue problems (polynomial eigenvalue problems where the coefficient matrices form a palindrome). For arbitrary wave vectors it is more challenging to solve. Finally, the proposed method may also be used for the analysis of locally resonant acoustic metamaterials. However, as their behavior does not depend on the lattice type, the benefit of being able to modify the outer boundary of the PUC is lost in this case.

The use of additional IGFEM nodes to prescribe periodic boundary conditions on non-conforming and immersed edges extends beyond the procedure described here for PnCs. In fact, a similar approach is used for the coupling between non-conforming meshes and contact, which is the subject of an incoming publication [56].

Declaration of competing interest

The authors declare that they have no known competing financial interests or personal relationships that could have appeared to influence the work reported in this paper.

Appendix. Constructing a transformation matrix for a simple 1-D PUC

The construction of the $\boldsymbol{T}$ matrix for a simple 1-D PUC as in Fig. 17 is explained in detail in this section. For simplicity, a very coarse mesh is used that is matching to the internal material interfaces. However, the extension to more complex problems in higher dimensions is straightforward.

In order to apply Bloch–Floquet boundary conditions on the two nodes shown as ○, the general condition

$$u(x_\mathrm{s}) = e^{\mathrm{i}k\cdot a}u(x_\mathrm{m}), \tag{34}$$

has to be satisfied, where $u(x_\mathrm{m})$ and $u(x_\mathrm{s})$ are displacements corresponding to the left and right enriched nodes, respectively. These nodes are separated by the lattice constant a. Using the IGFEM approximation, $u(x_\mathrm{m})$ and $u(x_\mathrm{s})$ are found as:

$$\begin{aligned} u(x_\mathrm{m}) &= N_1(x_\mathrm{m})U_1 + N_2(x_\mathrm{m})U_2 + s_\mathrm{m}\psi_\mathrm{m}(x_\mathrm{m})\alpha_\mathrm{m} \\ u(x_\mathrm{s}) &= N_3(x_\mathrm{s})U_3 + N_4(x_\mathrm{s})U_4 + s_\mathrm{s}\psi_\mathrm{s}(x_\mathrm{s})\alpha_\mathrm{s} \end{aligned} \tag{35}$$

Substituting Eq. (35) into Eq. (34) yields

$$N_3(x_\mathrm{s})U_3 + N_4(x_\mathrm{s})U_4 + s_\mathrm{s}\psi_\mathrm{s}(x_\mathrm{s})\alpha_\mathrm{s} = e^{i\mathrm{k}\cdot a}\left(N_1(x_\mathrm{m})U_1 + N_2(x_\mathrm{m})U_2 + s_\mathrm{m}\psi_\mathrm{m}(x_\mathrm{m})\alpha_\mathrm{m}\right), \tag{36}$$

which can then be rewritten as

$$\alpha_\mathrm{s} = \frac{e^{i\mathrm{k}\cdot a}}{s_\mathrm{s}\psi_\mathrm{s}(x_\mathrm{s})}\left(N_1(x_\mathrm{m})U_1 + N_2(x_\mathrm{m})U_2 + s_\mathrm{m}\psi_\mathrm{m}(x_\mathrm{m})\alpha_\mathrm{m}\right) - \frac{1}{s_\mathrm{s}\psi_\mathrm{s}(x_\mathrm{s})}\left(N_3(x_\mathrm{s})U_3 + N_4(x_\mathrm{s})U_4\right). \tag{37}$$

Written in the form $\boldsymbol{U} = \boldsymbol{T}\bar{\boldsymbol{U}}$, using a transformation matrix $\boldsymbol{T}$, the enriched subordinate DOF α_s can be eliminated:

$$\begin{bmatrix} U_1 \\ U_2 \\ U_3 \\ U_4 \\ \alpha_\mathrm{m} \\ \alpha_\mathrm{s} \end{bmatrix} = \begin{bmatrix} 1 & 0 & 0 & 0 & 0 \\ 0 & 1 & 0 & 0 & 0 \\ 0 & 0 & 1 & 0 & 0 \\ 0 & 0 & 0 & 1 & 0 \\ 0 & 0 & 0 & 0 & 1 \\ e^{i\mathrm{k}\cdot a}\frac{N_1(x_\mathrm{m})}{s_\mathrm{s}\psi_\mathrm{s}(x_\mathrm{s})} & e^{i\mathrm{k}\cdot a}\frac{N_2(x_\mathrm{m})}{s_\mathrm{s}\psi_\mathrm{s}(x_\mathrm{s})} & \frac{N_3(x_\mathrm{s})}{s_\mathrm{s}\psi_\mathrm{s}(x_\mathrm{s})} & \frac{N_4(x_\mathrm{s})}{s_\mathrm{s}\psi_\mathrm{s}(x_\mathrm{s})} & e^{i\mathrm{k}\cdot a}\frac{s_\mathrm{m}\psi_\mathrm{m}(x_\mathrm{m})}{s_\mathrm{s}\psi_\mathrm{s}(x_\mathrm{s})} \end{bmatrix} \begin{bmatrix} U_1 \\ U_2 \\ U_3 \\ U_4 \\ \alpha_\mathrm{m} \end{bmatrix}. \tag{38}$$

References

[1] G. Yi, B.D. Youn, A comprehensive survey on topology optimization of phononic crystals, Struct. Multidiscip. Optim. 54 (5) (2016) 1315–1344.

[2] W. Li, F. Meng, Y. Chen, Y.f. Li, X. Huang, Topology optimization of photonic and phononic crystals and metamaterials: A review, Adv. Theory Simul. 2 (7) (2019) 1900017.

[3] A.A. Mokhtari, Y. Lu, A. Srivastava, On the emergence of negative effective density and modulus in 2-phase phononic crystals, J. Mech. Phys. Solids 126 (2019) 256–271.

[4] B. Davis, M. Hussein, Nanophononic metamaterial: Thermal conductivity reduction by local resonance, Phys. Rev. Lett. 112 (5) (2014).

[5] Y. Yan, Z. Cheng, F. Menq, Y. Mo, Y. Tang, Z. Shi, Smart Mater. Struct. 24 (7) (2015) 075006.

[6] R. Lucklum, J. Li, Phononic crystals for liquid sensor applications, Meas. Sci. Technol. 20 (12) (2009) 124014.

[7] A. Oseev, M. Zubtsov, R. Lucklum, Gasoline properties determination with phononic crystal cavity sensor, Sensors Actuators B 189 (2013) 208–212.

[8] C.J. Rupp, M.L. Dunn, K. Maute, Switchable phononic wave filtering, guiding, harvesting, and actuating in polarization-patterned piezoelectric solids, Appl. Phys. Lett. 96 (11) (2010) 111902.

[9] R. Chaunsali, M. Toles, J. Yang, E. Kim, Extreme control of impulse transmission by cylinder-based nonlinear phononic crystals, J. Mech. Phys. Solids 107 (2017) 21–32.

[10] K.L. Manktelow, M.J. Leamy, M. Ruzzene, Topology design and optimization of nonlinear periodic materials, J. Mech. Phys. Solids 61 (12) (2013) 2433–2453.

[11] H. Nassar, X. Xu, A. Norris, G. Huang, Modulated phononic crystals: Non-reciprocal wave propagation and Willis materials, J. Mech. Phys. Solids 101 (2017) 10–29.

[12] I.A. Veres, T. Berer, O. Matsuda, Complex band structures of two dimensional phononic crystals: Analysis by the finite element method, J. Appl. Phys. 114 (8) (2013) 083519.

[13] F.-L. Li, Y.-S. Wang, C. Zhang, G.-L. Yu, Bandgap calculations of two-dimensional solid–fluid phononic crystals with the boundary element method, Wave Motion 50 (3) (2013) 525–541.

[14] F.-L. Li, Y.-S. Wang, C. Zhang, G.-L. Yu, Boundary element method for band gap calculations of two-dimensional solid phononic crystals, Eng. Anal. Bound. Elem. 37 (2) (2013) 225–235.

[15] H. Isakari, T. Takahashi, T. Matsumoto, Periodic band structure calculation by the Sakurai-Sugiura method with a fast direct solver for the boundary element method with the fast multipole representation, Eng. Anal. Bound. Elem. 68 (2016) 42–53.

[16] Y. Tanaka, Y. Tomoyasu, S.-i. Tamura, Band structure of acoustic waves in phononic lattices: Two-dimensional composites with large acoustic mismatch, Phys. Rev. B 62 (2000) 7387–7392.

[17] X.-X. Su, J.-B. Li, Y.-S. Wang, A postprocessing method based on high-resolution spectral estimation for {FDTD} calculation of phononic band structures, Physica B 405 (10) (2010) 2444–2449.

[18] E.N. Economou, M.M. Sigalas, Classical wave propagation in periodic structures: Cermet versus network topology, Phys. Rev. B 48 (1993) 13434–13438.

[19] M.S. Kushwaha, P. Halevi, G. Martínez, L. Dobrzynski, B. Djafari-Rouhani, Theory of acoustic band structure of periodic elastic composites, Phys. Rev. B 49 (1994) 2313–2322.

[20] A.A. Kutsenko, A.L. Shuvalov, A.N. Norris, Evaluation of the effective speed of sound in phononic crystals by the monodromy matrix method (L), J. Acoust. Soc. Am. 130 (6) (2011) 3553–3557.

[21] A. Kutsenko, A. Shuvalov, A. Norris, On the quasistatic effective elastic moduli for elastic waves in three-dimensional phononic crystals, J. Mech. Phys. Solids 61 (11) (2013) 2260–2272.

[22] L. Shi, N. Liu, J. Zhou, Y. Zhou, J. Wang, Q.H. Liu, Spectral element method for band-structure calculations of 3D phononic crystals, J. Phys. D: Appl. Phys. 49 (45) (2016) 455102.

[23] R. Alberdi, G. Zhang, K. Khandelwal, An isogeometric approach for analysis of phononic crystals and elastic metamaterials with complex geometries, Comput. Mech. 62 (3) (2018) 285–307.

[24] H. Zheng, C. Zhang, Y. Wang, J. Sladek, V. Sladek, A meshfree local RBF collocation method for anti-plane transverse elastic wave propagation analysis in 2D phononic crystals, J. Comput. Phys. 305 (2016) 997–1014.

[25] H. Nassar, Q.-C. He, N. Auffray, A generalized theory of elastodynamic homogenization for periodic media, Int. J. Solids Struct. 84 (2016) 139–146.

[26] A. Sridhar, V. Kouznetsova, M. Geers, A general multiscale framework for the emergent effective elastodynamics of metamaterials, J. Mech. Phys. Solids 111 (2018) 414–433.

[27] R. Hu, C. Oskay, Multiscale nonlocal effective medium model for in-plane elastic wave dispersion and attenuation in periodic composites, J. Mech. Phys. Solids 124 (2019) 220–243.

[28] L. Wang, H. Zheng, X. Lu, L. Shi, A Petrov-Galerkin finite element interface method for interface problems with bloch-periodic boundary conditions and its application in phononic crystals, J. Comput. Phys. 393 (2019) 117–138.

[29] N. Moës, J. Dolbow, T. Belytschko, A finite element method for crack growth without remeshing, Internat. J. Numer. Methods Engrg. 46 (1) (1999) 131–150.

[30] C. Duarte, I. Babuška, J. Oden, Generalized finite element methods for three-dimensional structural mechanics problems, Comput. Struct. 77 (2) (2000) 215–232.

[31] J. Zhao, Y. Li, W.K. Liu, Predicting band structure of 3D mechanical metamaterials with complex geometry via XFEM, Comput. Mech. 55 (4) (2015) 659–672.

[32] A. Cuba-Ramos, A.M. Aragón, S. Soghrati, P.H. Geubelle, J.-F. Molinari, A new formulation for imposing Dirichlet boundary conditions on non-matching meshes, Internat. J. Numer. Methods Engrg. 103 (6) (2015) 430–444.

[33] J.D. Sanders, J.E. Dolbow, T.A. Laursen, On methods for stabilizing constraints over enriched interfaces in elasticity, Internat. J. Numer. Methods Engrg. 78 (9) (2009) 1009–1036.

[34] N. Sukumar, J.E. Pask, Classical and enriched finite element formulations for Bloch-periodic boundary conditions, Internat. J. Numer. Methods Engrg. 77 (8) (2009) 1121–1138.

[35] I. Babuška, U. Banerjee, Stable generalized finite element method (SGFEM), Comput. Methods Appl. Mech. Engrg. 201–204 (2012) 91–111.

[36] V. Gupta, C. Duarte, I. Babuška, U. Banerjee, A stable and optimally convergent generalized FEM (SGFEM) for linear elastic fracture mechanics, Comput. Methods Appl. Mech. Engrg. 266 (2013) 23–39.

[37] K. Kergrene, I. Babuška, U. Banerjee, Stable generalized finite element method and associated iterative schemes; application to interface problems, Comput. Methods Appl. Mech. Engrg. 305 (2016) 1–36.

[38] T.P. Fries, A corrected XFEM approximation without problems in blending elements, Internat. J. Numer. Methods Engrg. 75 (5) (2008) 503–532.

[39] S. Soghrati, A.M. Aragón, C.A. Duarte, P.H. Geubelle, An interface-enriched generalized FEM for problems with discontinuous gradient fields, Internat. J. Numer. Methods Engrg. 89 (8) (2012) 991–1008.

[40] S. Soghrati, Hierarchical interface-enriched finite element method: An automated technique for mesh-independent simulations, J. Comput. Phys. 275 (2014) 41–52.

[41] A.M. Aragón, A. Simone, The discontinuity-enriched finite element method, Internat. J. Numer. Methods Engrg. 112 (11) (2017) 1589–1613.

[42] J. Zhang, S.J. van den Boom, F. van Keulen, A.M. Aragón, A stable discontinuity-enriched finite element method for 3-D problems containing weak and strong discontinuities, Comput. Methods Appl. Mech. Engrg. 355 (2019) 1097–1123.

[43] S.J. van den Boom, J. Zhang, F. van Keulen, A.M. Aragón, A stable interface-enriched formulation for immersed domains with strong enforcement of essential boundary conditions, Internat. J. Numer. Methods Engrg. 120 (10) (2019) 1163–1183.

[44] M.H.Y. Tan, P.H. Geubelle, 3D dimensionally reduced modeling and gradient-based optimization of microchannel cooling networks, Comput. Methods Appl. Mech. Engrg. 323 (2017) 230–249.

[45] M.H.Y. Tan, A.R. Najafi, S.J. Pety, S.R. White, P.H. Geubelle, Multi-objective design of microvascular panels for battery cooling applications, Appl. Therm. Eng. 135 (2018) 145–157.

[46] M.H.Y. Tan, D. Bunce, A.R.M. Ghosh, P.H. Geubelle, Computational design of microvascular radiative cooling pasonels for nanosatellites, J. Thermophys. Heat Transfer 32 (3) (2018) 605–616.

[47] R. Pejman, S.H. Aboubakr, W.H. Martin, U. Devi, M.H.Y. Tan, J.F. Patrick, A.R. Najafi, Gradient-based hybrid topology/shape optimization of bioinspired microvascular composites, Int. J. Heat Mass Transfer 144 (2019) 118606.

[48] A.R. Najafi, M. Safdari, D.A. Tortorelli, P.H. Geubelle, Shape optimization using a NURBS-based interface-enriched generalized FEM, Internat. J. Numer. Methods Engrg. 111 (10) (2017) 927–954.

[49] S.J. van den Boom, J. Zhang, F. van Keulen, A.M. Aragón, An interface-enriched generalized finite element method for level set-based topology optimization, Struct. Multidiscip. Optim. 68 (2020) 1–20.

[50] E. De Lazzari, S.J. van den Boom, J. Zhang, F. van Keulen, A.M. Aragón, A critical view on the use of NURBS to improve geometry representation in enriched finite element methods, Internat. J. Numer. Methods Engrg. 122 (5) (2020) 1195–1216.

[51] A.M. Aragón, B. Liang, H. Ahmadian, S. Soghrati, On the stability and interpolating properties of the hierarchical interface-enriched finite element method, Comput. Methods Appl. Mech. Engrg. 362 (2020) 112671.

[52] L. Brillouin, Les électrons dans les métaux et le classement des ondes de de Broglie correspondantes, C. R. Hebd. Seances Acad. Sci. (1930) 191–192.

[53] R.B. Nielsen, S.V. Sorokin, Periodicity effects of axial waves in elastic compound rods, J. Sound Vib. 353 (2015) 135–149.

[54] S. Soghrati, A. Nagarajan, B. Liang, Conforming to interface structured adaptive mesh refinement: New technique for the automated modeling of materials with complex microstructures, Finite Elem. Anal. Des. 125 (2017) 24–40.

[55] A. Nagarajan, S. Soghrati, Conforming to interface structured adaptive mesh refinement: 3D algorithm and implementation, Comput. Mech. 62 (5) (2018) 1213–1238.

[56] D. Liu, S.J. van den Boom, A. Simone, A.M. Aragón, An interface-enriched generalized finite element formulation for locking-free coupling of non-conforming discretizations and contact, 2021, submitted for publication.